

Interpreting Helioseismic Structure Inversion Results of Solar Active Regions

Chia-Hsien Lin^{1a,2} · Sarbani Basu^{1b} ·
Linghuai Li^{1c}

Received: ●●●●●●●● / Accepted: ●●●●●●●● / Published online: ●●●●●●●●

Abstract Helioseismic techniques such as ring-diagram analysis have often been used to determine the subsurface structural differences between solar active and quiet regions. Results obtained by inverting the frequency differences between the regions are usually interpreted as the sound-speed differences between them. These in turn are used as a measure of temperature and magnetic-field strength differences between the two regions. In this paper we first show that the “sound-speed” difference obtained from inversions is actually a combination of sound-speed difference and a magnetic component. Hence, the inversion result is not directly related to the thermal structure. Next, using solar models that include magnetic fields, we develop a formulation to use the inversion results to infer the differences in the magnetic and thermal structures between active and quiet regions. We then apply our technique to existing structure inversion results for different pairs of active and quiet regions. We find that the effect of magnetic fields is strongest in a shallow region above $0.985R_{\odot}$ and that the strengths of magnetic-field effects at the surface and in the deeper ($r < 0.98R_{\odot}$) layers are inversely related, *i.e.*, the stronger the surface magnetic field the smaller the magnetic effects in the deeper layers, and *vice versa*. We also find that the magnetic effects in the deeper layers are the strongest in the quiet regions, consistent with the fact that these are basically regions with weakest magnetic fields at the surface. Because the quiet regions were selected to precede or follow their companion active regions, the results could have implications about the evolution of magnetic fields under active regions.

Keywords: Sun: interior; Sun: magnetic fields; Sun: active regions; Sun: local helioseismology

1. Introduction

The availability of high-precision helioseismic data and the advancement of local helioseismology techniques have enabled investigations of fine details of solar internal

¹ Department of Astronomy, Yale University, P.O. Box
208101, New Haven, CT 06520-8101, USA
email a: linc@tcd.ie
email b: sarbani.basu@yale.edu
email c: li@astro.yale.edu

² School of Physics, Trinity College Dublin, Dublin 2, Ireland

dynamics for small regions of the Sun. Some of the methods, such as ring-diagram and time-distance analyses, have also enabled us examine details of the structure below solar active regions.

Ring-diagram analysis (Hill, 1988; Patron *et al.*, 1997) is used to determine frequencies of short-wavelength (high degree) modes in a small region of the Sun. These are modes that can be approximated as plane waves over a small area of the Sun. These frequencies can be inverted to determine the structure of the region under study using the same techniques that are used to invert global modes to study the spherically symmetric part of the solar structure. To avoid systematic errors, structure inversions are usually done using frequency differences between two regions to determine the difference in structure between the two regions (*e.g.*, Basu, Antia and Bogart, 2004, 2007). Time-distance helioseismology (Duvall *et al.*, 1993) measures the variations in the travel time of acoustic waves. The travel-time variations can then be used to infer the variations in the wave speed and flow velocity through an inversion procedure (*e.g.*, Kosovichev, Duvall, and Scherrer, 2000; Kosovichev, Duvall, and Birch, 2001).

Basu, Antia, and Bogart (2004) inverted the frequency differences between several active regions and nearby quiet regions to determine the sound-speed difference and the difference in the adiabatic index Γ_1 between these pairs of regions. They found that for all the active region – quiet region pairs, the sound speed below the active regions was smaller than that of the quiet regions for about the first 7 Mm, and then the sound speed became larger in the active regions than in the quiet regions. A similar behavior was seen for the adiabatic index (Γ_1). Qualitatively similar results were obtained by Kosovichev, Duvall, and Scherrer (2000) and Kosovichev, Duvall, and Birch (2001) using time-distance analysis. Kosovichev, Duvall, and Scherrer (2000), Kosovichev, Duvall, and Birch (2001), and Basu, Antia, and Bogart (2004) interpreted the results in terms of a temperature difference, and alternatively as a difference in the magnetic field. However, by examining the Γ_1 differences, Basu, Antia, and Bogart (2004) also concluded that the results cannot be explained as being caused by temperature changes or magnetic fields alone.

The presence of magnetic fields can affect the frequencies of waves in two ways: Firstly, the magnetic fields change the thermodynamic structure (*i.e.*, pressure and temperature profiles) of the medium that the waves travel through, which, in turn, changes the frequencies of the waves. Secondly, the plasma waves are directly affected by the magnetic fields through the Lorentz force. In other words, the modification to the frequencies results from both structural and non-structural (*i.e.*, Lorentz force) effects of the magnetic fields. Since the two effects are inseparable in the observed frequencies, the “structures” revealed by the inversions could partly be the manifestations of the frequency difference caused by Lorentz force on wave propagation. In addition, the inversion kernels to-date have been derived from non-magnetic reference models. Since the structural variables of a magnetic model have both magnetic and non-magnetic (gas) components, it had been uncertain if an inversion using a non-magnetic reference model would reveal the whole or only the gas part of the structural change. By using solar models that include magnetic fields and inversion kernels computed from non-magnetic reference models, Lin, Li, and Basu (2006) showed that the “sound speed” revealed by the inversions in the presence of magnetic fields is in fact a combination of both sound speed ($c_g \equiv \sqrt{\Gamma_1 P_{\text{gas}}/\rho}$) and Alfvén speed ($c_A \equiv B/\sqrt{4\pi\rho}$). To distinguish this property from the actual sound speed, we call it “wave speed”, defined as $c_T \equiv \sqrt{\Gamma_1 P_T/\rho}$, where P_T is the

total pressure ($= P_{\text{gas}} + P_{\text{mag}}$, where $P_{\text{mag}} = B^2/8\pi$, B being the magnetic-field strength). While the speed of sound is directly related to temperature, there is no simple, direct relationship between the "wave speed" c_T and either temperature or magnetic fields. Hence, it has not been possible to determine the magnetic-field and temperature profiles below active regions with any degree of accuracy.

In this paper, we use solar models that include magnetic fields to first confirm the Lin, Li, and Basu (2006) results and then derive a practical way of using the wave speed and Γ_1 inversion results to determine the thermal and magnetic structural differences between active and quiet regions. After confirming the reliability of this method to infer the thermal and magnetic structures, we then apply it to the inversion results of Basu, Antia, and Bogart (2004).

The main limitation of our models is that they are one dimensional, and hence the form of magnetic fields allowed is quite restrictive. We cannot, for example, have toroidal magnetic fields or magnetic fields over restricted ranges of latitudes or longitudes. However, we are forced to use such models because the codes to construct self-consistent solar models with arbitrary magnetic fields do not yet exist. A consequence of using 1D models is that we are likely to overestimate the effect of magnetic fields on thermal transport. In the real, three-dimensional case, convection, when obstructed by a magnetic flux tube can bend around the tube, which is not possible in the 1D case.

The rest of the paper is organized as follows: We describe the magnetic models in Section 2. A brief description of the inversion technique and the inversion results obtained from pairs of models are given in Section 3. The strategy to link the inversion results and temperature and magnetic fields is derived in Section 4. We apply the strategy to solar data in Section 5, and discuss the results in Section 6. The result of an attempt to model the subsurface magnetic structure is presented in Section 7. We summarize our results in Section 8. It should be noted that although we apply our method to results from ring-diagram analyses, it can be applied to any helioseismic technique that can determine the adiabatic index (Γ_1) below active regions.

2. Models

Since ring-diagram analysis is a variant of global-mode analysis, we model the difference between quiet and active regions as the difference between a solar model with no magnetic fields and a solar model that contains magnetic fields and the associated effects. We use a modified version of YREC (the Yale Rotation and Evolution Code: Demarque *et al.*, 2008) to construct the models.

How magnetic effects are incorporated in the models has been described in detail by Li and Sofia (2001) and Li *et al.*, (2003). We give a brief overview here.

To compute the effects of the magnetic fields, two magnetic variables are introduced. They are the magnetic energy density ($\chi \equiv B^2/8\pi\rho$) which describes the magnetic perturbation strength, and the magnetic field direction [$\gamma \equiv (2B_t^2 + B_p^2)/B^2$] which accounts for the tensorial feature of the magnetic pressure. B_t and B_p are respectively the toroidal and poloidal components of the magnetic field. The magnetic pressure can then be expressed in terms of χ , γ , and ρ , that is, $P_{\text{mag}} = (\gamma - 1)\chi\rho = B_t^2/8\pi$, in which the fact that the pressure is a tensor in the presence of magnetic fields has been taken into account.

With the addition of the magnetic variables, the equations of magnetic models are as following (Lydon and Sofia, 1995; Li and Sofia, 2001; Li *et al.*, 2003):

$$\frac{\partial P_T}{\partial M_r} = -\frac{GM_r}{4\pi r^4} - \frac{1}{4\pi r^2} \frac{\partial^2 r}{\partial t^2}, \quad (1)$$

$$\frac{\partial r}{\partial M_r} = \frac{1}{4\pi r^2 \rho}, \quad (2)$$

$$\frac{\partial L}{\partial M_r} = \epsilon - T \frac{dS_T}{dt} - \frac{1}{\rho} \frac{\partial u}{\partial t}, \quad (3)$$

$$\frac{\partial T}{\partial M_r} = -\frac{T}{P_T} \frac{GM_r}{4\pi r^4} \nabla, \quad (4)$$

and the first law of thermodynamics becomes:

$$TdS_T = dQ_T = dU_T + P_T dV - (\gamma - 1)(\chi/V)dV. \quad (5)$$

This modification thus affects the luminosity equation and the energy-transport equations (Equation 3 and Equation 4). In the above equations, M_r is the mass inside a radius r , ϵ is the energy generation rate, $u = aT^4$ is the radiation energy density (a being radiation constant), and ∇ is the dimensionless temperature gradient when magnetic fields are included.

These equations are similar to those governing non-magnetic models except that the pressure, total internal energy, and entropy now have a magnetic term, that is: $P_T = P_{\text{gas}} + P_{\text{mag}}$, $U_T = U + \chi$ and $S_T = S + \chi/T$. The solar models are constructed with OPAL opacities (Iglesias and Rogers, 1996) at high temperatures and Alexander and Ferguson (1994) opacities at low temperatures. Nuclear reaction rates of Bahcall and Pinsonneault (1992) were used. It should be noted that since we are dealing with the outermost layers of the model, the nuclear reaction rates only play an indirect role. The equation of state (EOS) of the gaseous phase is from OPAL (Rogers and Nayfonov, 2002). However, this has to be modified in the presence of magnetic fields. The equation of state is formally $\rho = \rho(P_T, T, \chi, \gamma)$, in addition to the usual dependence on chemical abundances:

$$\frac{d\rho}{\rho} = \alpha \frac{dP_T}{P_T} - \delta \frac{dT}{T} - \nu \frac{d\chi}{\chi} - \nu' \frac{d\gamma}{\gamma}, \quad (6)$$

plus terms due to composition. In the equation, α , δ , ν , and ν' are partial derivatives with respect to P_T , T , χ and γ , respectively.

Thus Equation 5 can be re-written as:

$$TdS_T = C_P dT - \frac{\delta}{\rho} dP_T + \left(1 + \frac{P_T \delta \nu}{\rho \alpha \chi}\right) d\chi + \frac{P_T \delta \nu'}{\rho \alpha \gamma} d\gamma. \quad (7)$$

The adiabatic index Γ_1 can be written in the same usual form, *i.e.*, $\Gamma_1 = 1/(\alpha - \delta \nabla'_{\text{ad}})$, where ∇'_{ad} is the modified adiabatic gradient and is given by

$$\nabla'_{\text{ad}} = \nabla_{\text{ad}} \left(1 - \frac{\nu \nabla_{\chi}}{\alpha} - \frac{\nu' \nabla_{\gamma}}{\alpha}\right), \quad (8)$$

where, as usual, $\nabla_{\text{ad}} = \partial \ln T / \partial \ln P_T = P_T \delta / \rho C_p T$, $\nabla_\chi = \partial \ln \chi / \partial \ln P_T$ and $\nabla_\gamma = \partial \ln \gamma / \partial \ln P_T$. The derivatives α , δ , and C_p change in the presence of magnetic fields.

The way that the EOS has been implemented is as follows: we determine “uncorrected” density [$\rho_0 = \rho_0(P_T, T)$] at a given chemical composition using the OPAL equation of state tables. The density is then corrected for the missing effects to obtain the actual density [$\rho = \rho_0 / (1 + \rho_0 \chi (\gamma - 1) / P_T)$]. We then calculate the changes in α , δ , and C_p caused by the presence of magnetic fields, and then use those to calculate Γ_1 . The changes in α , δ , and C_p also change energy transport. We use the mixing-length approximation, but with ∇_{ad} replaced by ∇'_{ad} and with the modified values of α , δ , C_p , *etc.* This modifies the properties of convection. There are also changes in the properties of convection. The details of including the magnetic effects in models can be found in Lydon and Sofia (1995), Li and Sofia (2001) and Li *et al.* (2003).

The magnetic profile of our models is specified by the distribution of χ . We have chosen a Gaussian profile for χ because a Gaussian profile has an unambiguous peak, its sphere of influence is well defined, and it has no discontinuities that can create havoc with both stellar structure and subsequent frequency calculations. Furthermore, other complex fields can be constructed by simply using several Gaussian profiles.

The Gaussian profile of χ is of the following form:

$$\chi = \chi_0 \exp\left[-\frac{1}{2}(M_D - M_{Dc})^2 / \sigma^2\right]. \quad (9)$$

$M_D \equiv \log[1 - M_r / M_\odot]$. M_{Dc} and σ are the adjustable parameters for the depth (in terms of M_D) of the peak of the magnetic field and the width (dimensionless) of the profile, respectively. $\chi_0 \equiv B_0^2 / 8\pi\rho_c$, in which B_0 is the tuning parameter for the peak magnetic field strength and ρ_c is the density at M_{Dc} .

In short, different magnetic models are only distinguished by their magnetic profiles, which are specified by three parameters: B_0 (peak strength), M_{Dc} (peak location) and σ (width).

Although this simple profile is implemented in most of our models to study the relation between the “wave speed” and the magnetic and thermal structures, we have also constructed other types of field profiles by using multiple Gaussians in order to check the validity of the relation in a complex field.

The relative differences of several structural parameters between a magnetic and a non-magnetic model are shown in Figure 1. We define $\beta \equiv P_{\text{mag}} / P_{\text{gas}}$. As $P_{\text{mag}} = 0$ in the non-magnetic reference model, $\delta\beta = \beta = P_{\text{mag}} / P_{\text{gas}}$ illustrates the magnetic configuration in the magnetic model in this case. It is plotted as a gray dashed line using the scale at the right side. We can see that $\delta c_g^2 / c^2$ and $\delta c_T^2 / c^2$ are very different ($c = c_T = c_g$ in the non-magnetic reference model). The wave-speed difference ($\delta c_T^2 / c^2$) changes from negative to positive in the region of the magnetic fields while $\delta c_g^2 / c^2$ shows a single dip in the region. The positive and negative peaks of $\delta c_T^2 / c^2$ do not show any explicit correlation with the profile of the magnetic fields. Unsurprisingly, $\delta c_T^2 / c^2$, $\delta c_g^2 / c^2$, and $\delta T / T$ become almost identical at greater distances from the region of magnetic effects, which confirms that $\delta c_T^2 / c^2$ is indeed a good representation of temperature difference in non-magnetic regions. Another important feature is that, except for $\delta\Gamma_1 / \Gamma_1$, all variables show the influence of the magnetic field at large distances from the field. The $\delta\Gamma_1 / \Gamma_1$ profile approximately

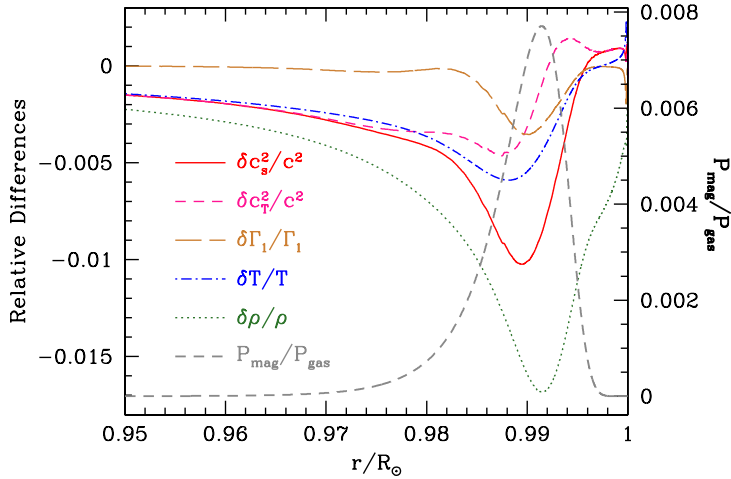


Figure 1. Differences between a magnetic and a non-magnetic model. Note that for the non-magnetic reference model, $c = c_T = c_g$. The gray dashed line shows the ratio of the magnetic to gas pressure, and the value can be read from the right-hand ordinate.

follows the profile of β with no tail below the region of the magnetic fields. In other words, the magnetic effect on Γ_1 is fairly localized to the vicinity of the magnetic fields. Although the situation may change in two-dimensional models, where more realistic magnetic configurations are used, the basic features in the differences of the structure parameters are expected to remain the same.

3. Test Inversions

3.1. Inversion Procedure

The frequencies of solar oscillation modes depend on the solar structure. The starting point of helioseismic inversions is the linearization of the oscillation equations around a known solar model (the so-called reference model) using the variational principle. The frequency differences can then be related to the relative variations in sound speed (c) and density (ρ) either between two models or between the Sun and the reference model. The relation between the differences in frequency and these two variables (*i.e.*, c and ρ) can be written as (Dziembowski, Pamyatnykh and Sienkiewicz, 1990; Antia and Basu, 1994):

$$\frac{\delta\omega_i}{\omega_i} = \int_0^R K_{c^2,\rho}^i(r) \frac{\delta c^2}{c^2}(r) dr + \int_0^R K_{\rho,c^2}^i(r) \frac{\delta\rho}{\rho}(r) dr + \frac{F_{\text{surf}}(\omega_i)}{E_i} + \epsilon_i, \quad (10)$$

where c is the adiabatic sound speed, K^i are the kernels and are known functions of the reference model, $\delta\omega_i/\omega_i$ is the relative frequency difference of the i th mode, ϵ_i is the observational error in $\delta\omega_i/\omega_i$, and $F_{\text{surf}}(\omega_i)/E_i$, usually called the “surface term”, represents the effect of uncertainties in the model close to the surface. Here, E_i is a measure of the mode inertia. Other pairs of variables such as (Γ_1, ρ) can be

used instead of the (c^2, ρ) pair used above. There are several techniques that can be used to invert Equation 10. The inversion results used in this paper were obtained using the Subtractive Optimally Localized Averages (SOLA) technique (Pijpers and Thompson, 1992, 1994). The details of the inversion procedure and the quality of the averaging kernels were shown in Basu, Antia, and Bogart (2004).

Basu, Antia, and Bogart (2004) inverted the frequency differences between active and quiet regions, instead of between active regions and a solar model. One of the reasons for doing so was to reduce foreshortening effects. The projection of the spherical solar surface onto a flat map introduces some foreshortening that depends on the distance of the region from the disc center, which can cause systematic errors in determining the mode characteristics. By selecting comparison regions at the similar latitudes and tracking both in time intervals symmetric about their central meridian passages (CMP), the authors assured that the foreshortening effects in both regions are nearly identical, and, hence, the effect is eliminated to a large degree by taking the difference. Such a difference also reduces the so-called “surface term” in the inversion. A large part of the surface term in frequency differences between solar models and the Sun arises from shortcomings in modeling the near-surface layers of the Sun. Since the featured inversions are for two sets of solar frequency differences, the surface term is much smaller, and only one surface term suffices. The accuracy of their inversion results were ensured by the consistency between the the results from SOLA and the results from regularized least squares (RLS). It should be noted that the inversion kernels were calculated without any effect of the magnetic fields included, and as a result the “sound speed” inversions yield results that are a combination of the real sound speed difference and a magnetic component.

To simulate the aforementioned ring-diagram inversions, we use a non-magnetic model as the reference model. However, since quiet regions may also have magnetic fields in the deeper regions, we have also examined inversions between two magnetic models while still using non-magnetic kernels. We constructed a number of different magnetic models as the test models in order to determine $\delta c^2/c^2$, $\delta\Gamma_1/\Gamma_1$, and $\delta\rho/\rho$ between the magnetic models and the non-magnetic reference model. In order to estimate the errors in the inversion results that are caused by the errors in the observed frequencies, we select only those modes that are also present in the observational data. The observational data set we use for the mode selection is from Rhodes *et al.* (1998), which is based on 61 days of data collected by the *SOI/MDI* instruments beginning in May 1996. The data set contains f modes and p modes up to $\ell = 1000$. This set is much larger than data sets obtained from ring-diagram analyses. However, since our objective is merely to determine what variables are actually obtained by the usual “sound-speed” and Γ_1 inversions, a larger data set will not affect our conclusion. We have also used the 360-day mode-set from MDI (Schou, 1999).

3.2. Results

The magnetic effects on thermal structures are different at different depths. This is not only because the ratio of magnetic to gas pressure depends on the location, but also because any related changes in temperature can shift the position of the ionization zone. Hence, we need to examine the inversion results at different depths in order to investigate how the variations of magnetic profiles affect different structural properties (*i.e.*, c_g , c_T , Γ_1 , and ρ) and the difference between c_g and c_T , as well as to

determine whether or not the inversion can consistently and accurately reveal these properties under different magnetic situations.

In Figure 2 we show the results of “sound-speed” inversions for two cases. In panel (a) we show the inversion results when one of the models is non-magnetic, and in panel (b) we show the results of inverting the frequency differences between two magnetic models. In each case, the inversion kernels were from a non-magnetic model. The figure shows that what the inversion produces is not the usual “sound speed” difference, *i.e.*, difference of the quantity $c_g^2 = \Gamma_1 P_{\text{gas}}/\rho$, but a “wave speed” difference where the “wave speed” is defined as $c_T^2 = \Gamma_1 P_T/\rho$, thereby confirming the results of Lin, Li, and Basu (2006).

Figure 3 shows the inversion results of $\delta\Gamma_1/\Gamma_1$ [panel (a)] and $\delta\rho/\rho$ [panel (b)]. In both cases we used the same models as in Figure 2(b). Because the adiabatic index (Γ_1) is a function of the equation of state and because density (ρ) is an intrinsic property of gas, it is not sensible to split them into magnetic and non-magnetic components. $\delta\Gamma_1/\Gamma_1$ and $\delta\rho/\rho$ reflect the changes in the equations of state and in the gas distribution caused by the presence of magnetic fields. From Figure 3, we can see that the inversion results closely follow the computed values even though the inversion kernels were derived from a non-magnetic model. However, the errors in the $\delta\rho/\rho$ inversions are too large for the results to be useful. With the limited mode sets obtained from ring-diagram analysis, the errors would be even larger, and hence only in very rare cases can a proper density inversion be done.

Although the frequencies of both magnetic and non-magnetic models were computed from our pulsation code, which does not include the Lorentz-force effect, the effect of the absence is clearly not significant. If it were, the inversion results would have shown large deviations for models with different types of magnetic profiles since the direct effects on wave frequencies would be very different for different modes that have different lower turning points with respect to the field positions. Clearly, such deviations are not seen. The inversion results also show that the use of non-magnetic kernels do not lead to any significant errors in the inversion results and hence we are justified in using the results of Basu, Antia, and Bogart (2004).

Thus, the examples in Figures 2 and 3 show that the structural differences revealed by the inversions implemented with non-magnetic kernels are a combination of both direct magnetic effects and the gaseous structural changes.

4. Estimating Magnetic and Thermal Structure from Inversion Results

4.1. Mathematical Relation between Inversion Results and Magnetic Fields

The wave speed (c_T) is affected by both the magnetic fields and the thermal structures. In the following, we derive the relations between the relative wave-speed difference ($\delta c_T^2/c_T^2$) and the differences in the magnetic structures (represented by $\delta\beta$) and in the thermal structures (reflected in $\delta c_g^2/c_g^2$ or $\delta T/T - \delta\mu/\mu$). The subscripts 1 and 0 in the equations denote the test and reference models wherever there may be confusion. We should point out that the reference model in the following derivation can be either magnetic or non-magnetic. When $P_{\text{mag}_0} = 0$, we obtain the special case of a non-magnetic reference model.

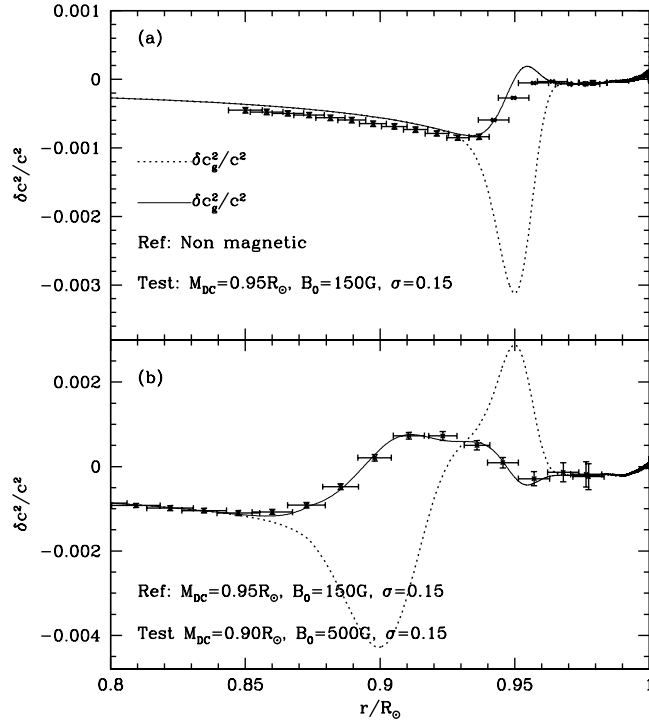


Figure 2. Comparison of the inverted $\delta c^2/c^2$ with the exact relative differences of the sound speed and of the wave speed. The dotted line is the sound-speed difference $[(c_g^2 - c_{\text{ref}}^2)/c_{\text{ref}}^2]$ and the solid line is wave speed difference $[(c_T^2 - c_{\text{ref}}^2)/c_{\text{ref}}^2]$, where c_{ref}^2 refers to c^2 of the reference model. Note that c_{ref} , c_T , and c_g are the same in the non-magnetic reference model. The parameters of the magnetic-field profile are indicated in each panel. The inverted values are plotted as symbols along with the error bars. The errors are obtained from the observational errors in the frequencies. The inversion in (a) are with the Rhodes *et al.* mode-set, the one in (b) is with the Schou (1999) set.

$$\begin{aligned}
 \frac{\delta c_T^2}{c_T^2} &= \frac{\delta \Gamma_1}{\Gamma_1} - \frac{\delta \rho}{\rho} + \frac{\delta P_T}{P_T} \\
 &= \frac{\delta \Gamma_1}{\Gamma_1} - \frac{\delta \rho}{\rho} + \frac{\delta P_{\text{gas}} + \delta P_{\text{mag}}}{P_{\text{gas}_0} + P_{\text{mag}_0}} \\
 &= \frac{\delta \Gamma_1}{\Gamma_1} - \frac{\delta \rho}{\rho} + \left(\frac{\delta P_{\text{gas}}}{P_{\text{gas}_0}} + \frac{\delta P_{\text{mag}}}{P_{\text{gas}_0}} \right) [1 + \beta_0]^{-1}, \quad (11)
 \end{aligned}$$

where $\beta_0 = P_{\text{mag}_0}/P_{\text{gas}_0}$ is the magnetic to gas pressure ratio in a reference model. The quantity $\delta P_{\text{mag}}/P_{\text{gas}_0}$ can be related to $\delta \beta = \delta(P_{\text{mag}}/P_{\text{gas}})$ as follows:

$$\delta \beta = \beta_1 - \beta_0 = \frac{P_{\text{mag}_1}}{P_{\text{gas}_1}} - \frac{P_{\text{mag}_0}}{P_{\text{gas}_0}}, \quad (12)$$

$$\frac{\delta P_{\text{mag}}}{P_{\text{gas}_0}} = \frac{P_{\text{mag}_1} - P_{\text{mag}_0}}{P_{\text{gas}_0}} = \delta \beta + \beta_1 \cdot \frac{\delta P_{\text{gas}}}{P_{\text{gas}_0}}. \quad (13)$$

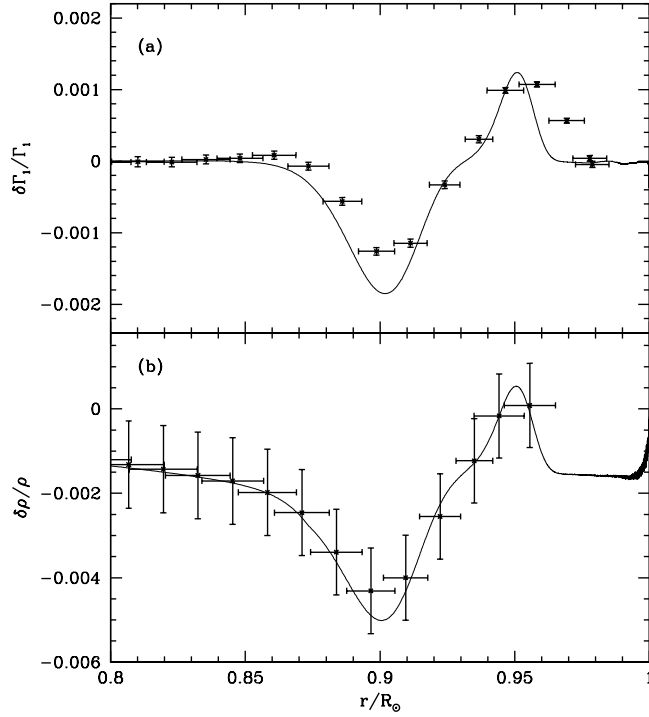


Figure 3. Inversion results for $\delta\Gamma_1/\Gamma_1$ (upper panel) and $\delta\rho/\rho$ (lower panel). In both panels, the solid line is the exact difference between the magnetic model and the reference model (*cf.* Figure 2(b) for details of the models). The inverted results are plotted as symbols along with the error bars. The errors are obtained from the observational errors of the modes used in the inversion. The inversions are with the Schou (1999) mode set.

By using Equation (13) and assuming $\beta_1 \ll 1$ and $\beta_0 \ll 1$, Equation (11) becomes:

$$\frac{\delta c_T^2}{c_T^2} \approx \frac{\delta\Gamma_1}{\Gamma_1} - \frac{\delta\rho}{\rho} + \frac{\delta P_{\text{gas}}}{P_{\text{gas}}} + \delta\beta\left(1 + \frac{\delta P_{\text{gas}}}{P_{\text{gas}}}\right) = \frac{\delta c_g^2}{c_g^2} + \delta\beta\left(1 + \frac{\delta P_{\text{gas}}}{P_{\text{gas}}}\right), \quad (14)$$

which can also be expressed in the following form:

$$\frac{\delta c_T^2}{c_T^2} \approx \frac{\delta\Gamma_1}{\Gamma_1} + \frac{\delta T}{T} - \frac{\delta\mu}{\mu} + \delta\beta\left(1 + \frac{\delta P_{\text{gas}}}{P_{\text{gas}}}\right) \quad (15)$$

by using the relation $P/\rho \propto T/\mu$. Although $P/\rho \propto T/\mu$ is the same form as the equation of state for an ideal gas, we are assuming that all non-ideal effects are incorporated in the term μ . While μ is therefore not strictly the mean molecular weight in the above equations, this allows us to express the sound speed as above and allows Equations (14) and (15) to be valid in non-ideal gas situations. It is in fact a standard procedure to modify μ in the region of our study because the main non-ideal effect in this region is ionization.

As can be seen from Equations (14) and (15), $\delta c_T^2/c_T^2$ results from not only the magnetic effects but also the difference in the sound speed, which represents the

difference in the gas structure. When the magnitude of $\delta\beta$ is comparable to the magnitudes of other differences in Equation (15), $\delta c_T^2/c_T^2 - \delta\Gamma_1/\Gamma_1$ should not be interpreted as the temperature difference. Nevertheless, if $\delta\beta$ can be determined and if $\delta P_{\text{gas}}/P_{\text{gas}} \ll 1$, we can obtain the relative difference in both sound speed and stratification:

$$\frac{\delta c_g^2}{c_g^2} \approx \frac{\delta c_T^2}{c_T^2} - \delta\beta \quad (16)$$

$$\frac{\delta T}{T} - \frac{\delta\mu}{\mu} \approx \frac{\delta c_T^2}{c_T^2} - \frac{\delta\Gamma_1}{\Gamma_1} - \delta\beta \quad (17)$$

4.2. Procedure to infer Magnetic and Thermal Structures

Investigations of the structure of active regions are usually based on the assumption that the “sound-speed” inversion results are a good measure of the actual sound-speed difference between active and quiet regions. Under such assumption, $\delta c^2/c^2$ is considered as due entirely to the magnetic fields while $\delta c^2/c^2 - \delta\Gamma_1/\Gamma_1$ is interpreted as difference in temperatures. Although such interpretations may give qualitatively correct results, they are not quantitatively correct, as demonstrated by Equations (14) and (15). While it is true that in general a lower wave speed implies a lower temperature, the quantitative relationship is less direct. Since $\delta\Gamma_1/\Gamma_1$ follows the distribution of the magnetic field (see Figure 1), we explore the possibility of obtaining a relation between $\delta\beta$ and $\delta\Gamma_1/\Gamma_1$. In the region where ring-diagram inversion is valid (approximately $0.975R_\odot$ to $0.992R_\odot$), the effort is complicated by the fact that the region is an ionization zone and that Γ_1 changes as a result of ionization. The presence of magnetic fields will change the temperature profile, which in turn leads to shifting of ionization zones and thereby a change in μ at each depth. Consequently, any relation we find between $\delta\beta$ and $\delta\Gamma_1/\Gamma_1$ is likely to depend on depth.

For the purpose of determining the relation between $\delta\beta$ and $\delta\Gamma_1/\Gamma_1$, we have constructed a large number of magnetic models by adjusting the three parameters (B_0 , M_{Dc} , and σ) of the magnetic profile, as described in Section 2. The values of these parameters range from 10 to 1000G for B_0 , $0.9R_\odot$ to $0.998R_\odot$ for the location of peak and 0.1 to 0.9 for the width parameter. In order to validate any relation that we might obtain, we have also constructed several models with more complex magnetic fields using multiple Gaussian profiles.

Figure 4 shows $\delta\Gamma_1/\Gamma_1$ versus $\delta\beta$ at different depths. Since the values of $\delta\Gamma_1/\Gamma_1$ obtained from the inversions by Basu, Antia, and Bogart (2004) range from negative to positive, we need to investigate the relation between $\delta\beta$ and $\delta\Gamma_1/\Gamma_1$ for both positive and negative $\delta\Gamma_1/\Gamma_1$. For this purpose, we created negative (positive) $\delta\Gamma_1/\Gamma_1$ by using non-magnetic (magnetic) models as the reference and magnetic (non-magnetic) models as the test model. In Figure 4, we plotted negative (positive) $\delta\Gamma_1/\Gamma_1$ versus $\delta\beta$ in the upper (lower) two rows. In all panels, each diamond symbol represents the computed values ($\delta\Gamma_1/\Gamma_1$, $\delta\beta$) of a model pair at the depth indicated above each panel. The scale of abscissa is chosen to be comparable to the values of $\delta\Gamma_1/\Gamma_1$ from the inversions. The figure shows that while there is a tight relationship between $\delta\beta$ and $\delta\Gamma_1/\Gamma_1$ in the region $0.975R_\odot < r < 0.990R_\odot$, where the inversion is reliable, there is often no unique relation, but only an envelope, in the deeper and shallower layers. A closer examination of the models associated with the points located away

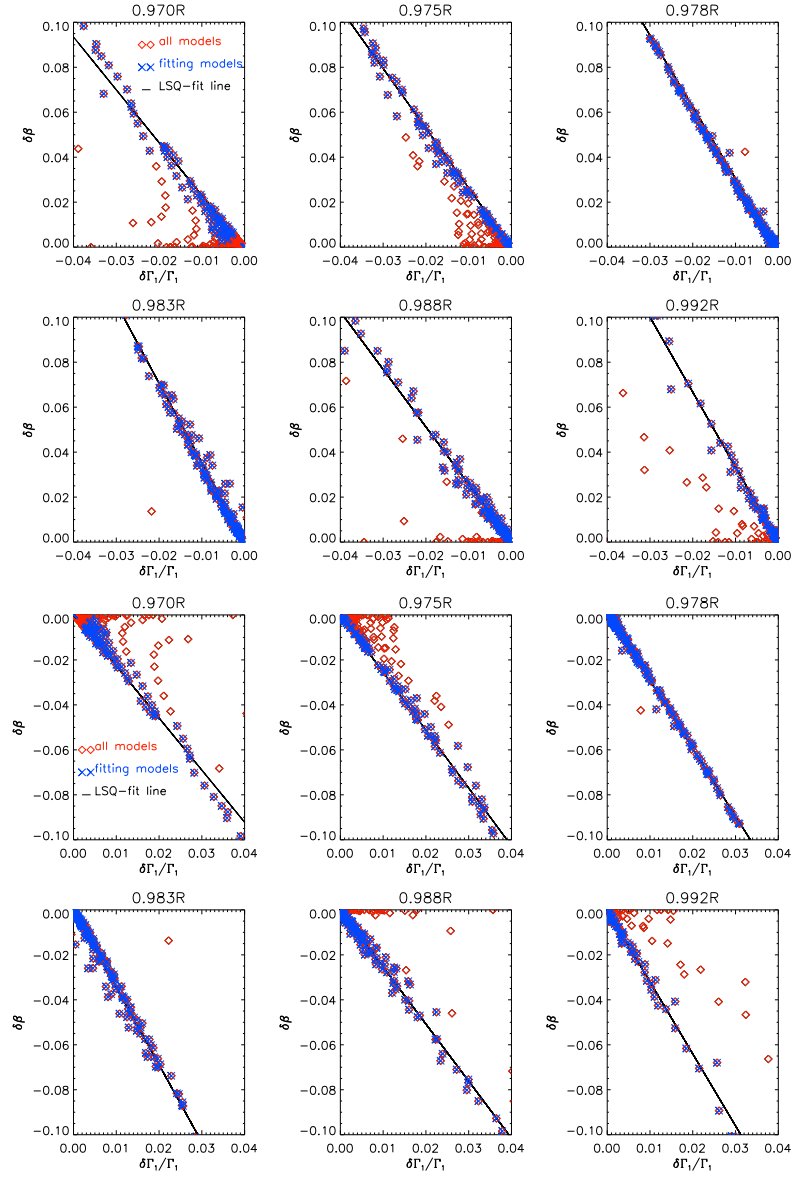


Figure 4. The $\delta\Gamma_1/\Gamma_1$ versus $\delta\beta$ relation at different depths. The upper two rows are the relations of magnetic model – non-magnetic model, and the lower two rows are the relations of non-magnetic model – magnetic models. Each diamond represents one model pair, or equivalently, a unique magnetic profile. The line is the result of a least squares fit (LSQ-fit) obtained after excluding some stray points. The crosses are the ones included for the fit.

from the envelope reveals that the $\delta\Gamma_1/\Gamma_1$ and $\delta c_T^2/c_T^2 - \delta\Gamma_1/\Gamma_1$ profiles resulting from these models are very different from the inversion results. For instance, the point in the panel of $0.97R_\odot$ whose $|\delta\Gamma_1/\Gamma_1|$ has a magnitude of approximately 0.012 and $|\delta\beta|$ roughly 0.005 belongs to the $\delta\Gamma_1/\Gamma_1$ profile with a peak magnitude greater than 0.1 at $0.985R_\odot$ (*cf.* Figure 5(g)). Other points that locate even further away from the envelope are produced by those $\delta\Gamma_1/\Gamma_1$ profiles with even larger peak magnitudes. However, the magnitudes of the inverted $\delta\Gamma_1/\Gamma_1$ shown in Basu, Antia, and Bogart (2004) are all less than 0.04. Thus, these stray points appear to result from unrealistic magnetic configurations, and hence, we do not use them to determine the relation. After removing these stray points, we applied a least squares fit (LSQ fit) to the rest of data to obtain a linear relation at each selected depth. The straight line in each panel is our fitted line, and is the relation between $\delta\beta$ and $\delta\Gamma_1/\Gamma_1$ at that depth to be used to infer $\delta\beta$ from the solar inversion results.

4.3. Validating the $\delta\beta - \delta\Gamma_1/\Gamma_1$ Relation

Using the known $\delta\Gamma_1/\Gamma_1$ between the test models and the reference models, we first determined $\delta\beta$ between the models based on the $\delta\beta - \delta\Gamma_1/\Gamma_1$ relation. Once $\delta\beta$ is determined, we then ventured to examine whether, and how accurately, $\delta c_g^2/c_g^2$ and $(\delta T/T - \delta\mu/\mu)$ can be inferred from $\delta c_T^2/c_T^2$, $\delta\Gamma_1/\Gamma_1$ and $\delta\beta$, as explained in Section 3.2 [*cf.* Equations (16) and (17)]. These quantities can then be compared with the exact differences between the models to assess the errors of the estimations. While $\delta\mu/\mu$ is negligible in the deeper regions where gas is almost fully ionized, it has to be taken into account at the vicinity of ionization zones, which are within the region we are probing. $\delta T/T$ and $\delta\mu/\mu$ can be separated only if it is assumed that we know the equation of state of solar matter correctly. We therefore, chose to determine $(\delta T/T - \delta\mu/\mu)$ rather than $\delta T/T$ in this paper to avoid possible errors from the equation of state.

Since the relation is obtained by removing several unrealistic models and using fairly simple magnetic-field configurations, we also need to assess the accuracy of the relationship under these excluded magnetic conditions. Hence, we applied the aforementioned steps to the test models with multiple-Gaussian magnetic profiles and the test models that result in those stray points in Figure 4. We also applied the procedure to infer $\delta c_g^2/c_g^2$, $\delta\beta$ and $(\delta T/T - \delta\mu/\mu)$ between two magnetic models, that is, both test and reference models are magnetic.

The results of the exercise are shown in Figure 5. Panels (a), (b), (c) are the results obtained by applying our relation to models with simple magnetic fields concentrated at different depths; panels (d) and (e) show two examples when both test and reference models are magnetic; (f) is a case of complex magnetic fields which is created by a double-Gaussian profile; and panels (g) and (h) show two model pairs that are excluded from our fitting. We can see that the reconstructed $\delta\beta$ (the red crosses) closely match the computed values (the dot-dash line). Even in the cases where $\delta\beta$ is reasonably complex, the simple relation still re-creates the $\delta\beta$ to an accuracy that is sufficient to apply to the solar results. As can be seen in the same figure, our estimated $\delta c_g^2/c_g^2$ (blue stars) and $(\delta T/T - \delta\mu/\mu)$ (green diamonds), still follow the exact values, but show slightly larger deviations in several cases, which is an indication that $\delta P_{\text{gas}}/P_{\text{gas}}$ between the test and reference models is not negligible in these cases. The results in panel (g) demonstrate how much the estimated and computed $\delta\beta$ would differ in the excluded model pairs.

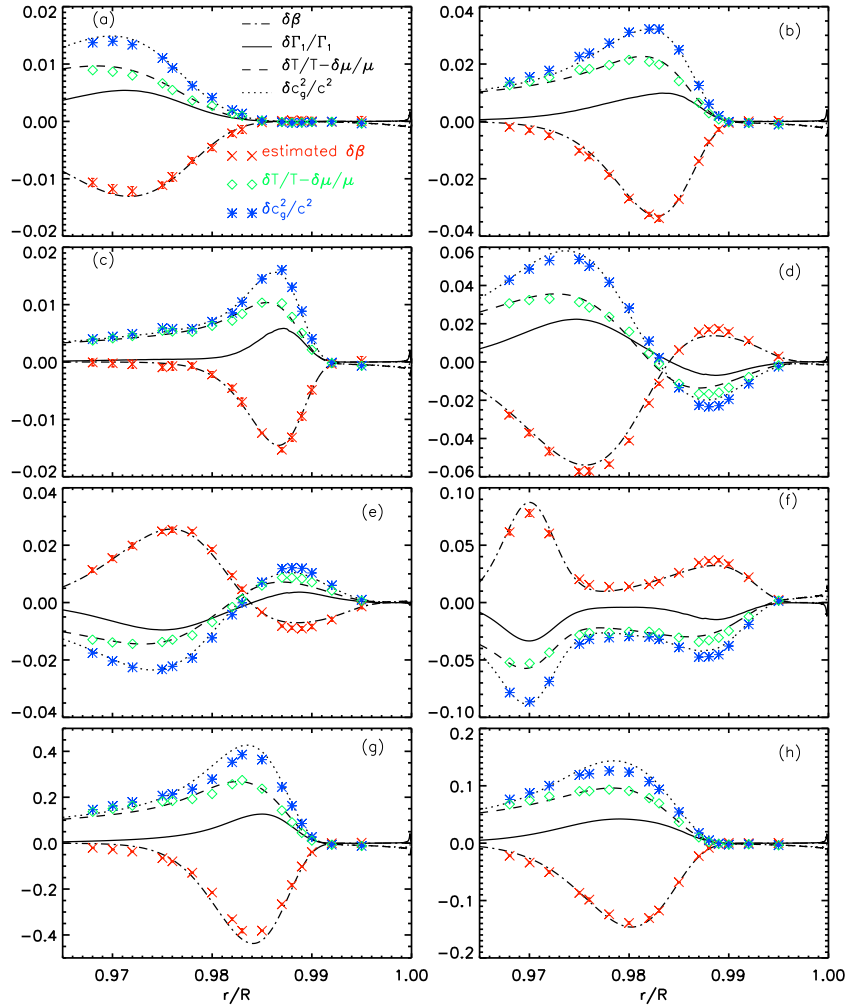


Figure 5. The result of applying the $\delta\Gamma_1/\Gamma_1 - \delta\beta$ relation to models. The symbols are the $\delta\beta$, $(\delta T/T - \delta\mu/\mu)$, and $\delta c_g^2/c_g^2$ determined by using the known values of $\delta\Gamma_1/\Gamma_1$, $\delta c_g^2/c_g^2 - \delta\Gamma_1/\Gamma_1$, and Equations (16) and (17). The exact values of the determined quantities are shown as continuous lines.

5. Application to Solar Data

Once the reliability of the relation was established, we applied it to the inversion results. Although the estimated $\delta T/T - \delta\mu/\mu$ and $\delta c_g^2/c_g^2$ are qualitatively correct in our model tests, the larger uncertainties in the real solar data may result in even more erroneous estimations. Hence, we shall only focus on $\delta\beta$ in the application to the solar data.

Table 1. Properties of the different pairs of regions that were analyzed

Pair No.	Lat. (deg.)	CM ^a Lon. (deg.)	Mag. Index (Gauss)	NOAA	Type (at CMP ^b)	Max. area (millionths)
1	7N	016	19.9	8040	β	150
		341	0.2			
2	16S	222	23.3	9904	β	60
		242	2.7			
3	11S	195	26.8	9896	α	110
		205	2.0			
4	14S	105	53.2	8518	β	170
		075	0.9			
5	18N	180	56.3	9899	β	220
		240	2.2			
6	21S	82	68.4	8193	β	290
		067	0.6			
7	19N	215	81.5	9893	$\beta\gamma\delta$	490
		255	0.7			
8	4N	013	86.9	9914	β	260
		028	1.1			
9	20N	204	108.5	9901	$\beta\gamma$	350
		249	0.7			
10	15S	150	125.8	9906	$\beta\gamma\delta$	850
		120	2.8			
11	20N	071	146.6	9026	$\beta\gamma\delta$	820
		126	0.9			
12	19N	147	241.6	9393	$\beta\gamma\delta$	2440
		207	1.2			

^a Central Meridian^b Central Meridian Passage

Basu, Antia, and Bogart (2004) determined $\delta c_T^2/c_T^2$ and $\delta\Gamma_1/\Gamma_1$ of twelve selected active region(AR) – quiet region(QS) pairs by using an inversion procedure with the frequencies determined by a ring-diagram analysis. The selected active regions were tracked while they were crossing the central meridian (CM). The QS in each pair was selected such that it also crossed the central meridian at the same latitude as the AR within the same Carrington rotation. In other words, the QS either preceded or followed the AR.

The magnetic-field strengths of the ARs scaled a wide range. The magnetic field strength of each region is defined by a magnetic activity index (MAI), which is an average of the absolute values of the strong fields ($|B_z| \geq 50$ G). Details of how the MAI for a region is calculated can be found in Basu, Antia, and Bogart (2004). Some of the properties of the regions are described in Table 1. The table is arranged in order of increasing MAI of the active region.

The estimated values of $\delta\beta$ (red crosses), along with the inversion results and error bars, for the different AR – QS pairs are plotted in Figures 6 and 7. The error bars are computed by propagating the errors from fitting and from the inversion results of $\delta\Gamma_1/\Gamma_1$ through the $\delta\beta - \delta\Gamma_1/\Gamma_1$ relationship derived in Section 4.2. The

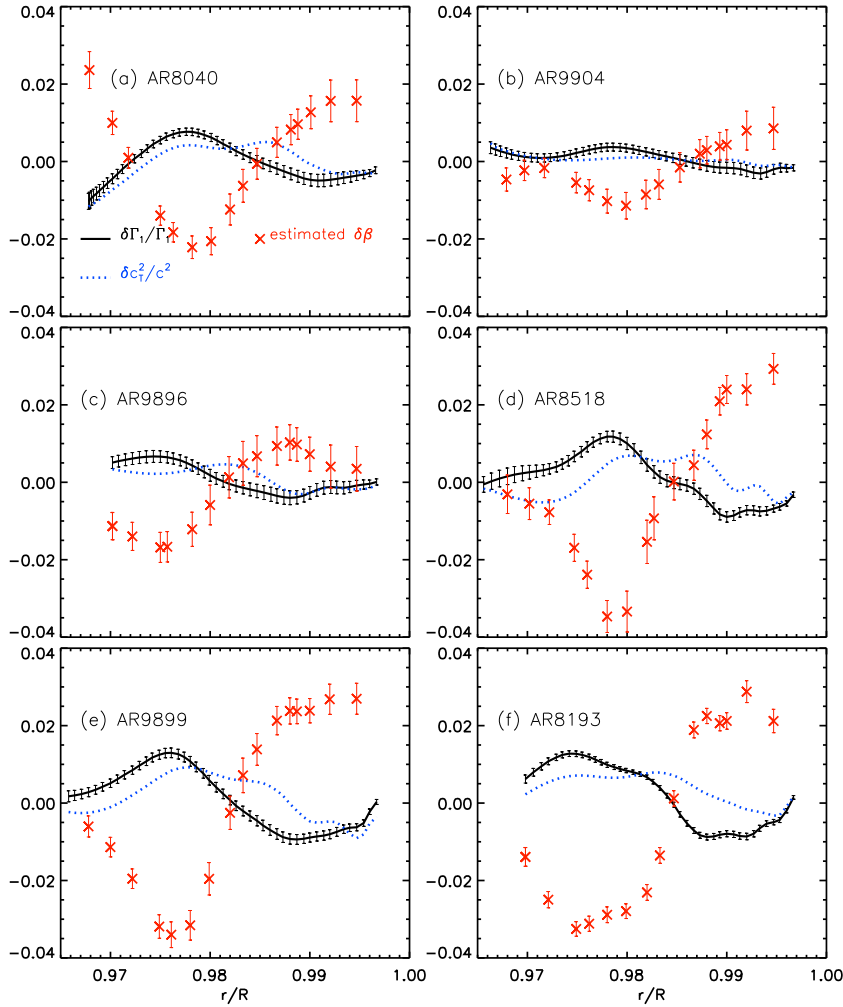


Figure 6. The estimated $\delta\beta$ between different pairs of solar active and quiet regions are plotted as red crosses along with the error bars. Also shown are the primary inversion results for $\delta\Gamma_1/\Gamma_1$ (solid line) and $\delta c_T^2/c_T^2$ (dotted line) obtained by Basu, Antia, and Bogart (2004). Because the error bars of $\delta\Gamma_1/\Gamma_1$ and of $\delta c_T^2/c_T^2$ are of similar magnitude, only the former are plotted for the sake of clarity.

figures show that in the region above approximately $0.985R_\odot$, $\delta\beta$ generally increases with increasing MAI. The only notable exceptions are AR 9026 and AR 9393. The anomalously low near-surface $\delta\beta$ of the strong active regions AR 9026 and AR 9393 is worth commenting upon. These two regions have the largest number of the flares among all the regions studied, 422 for AR 9026 and 568 for AR 9393. The next highest flare index is only 129 for AR 9906. It is therefore quite likely that the flaring activity

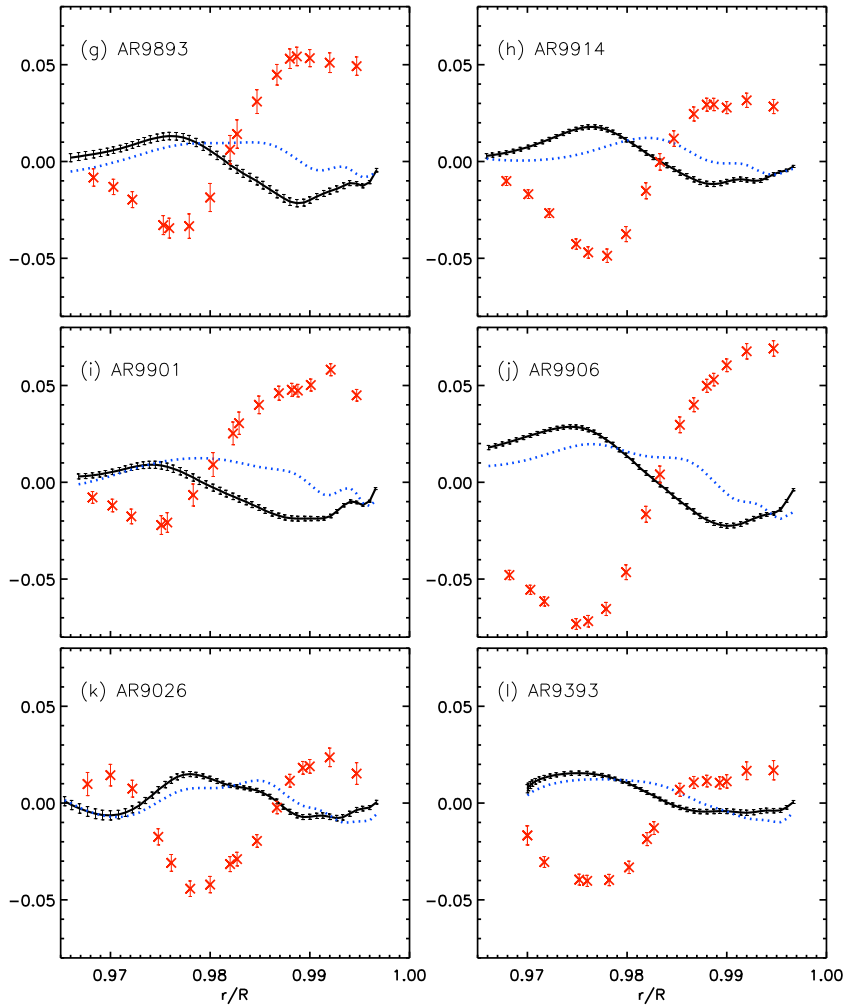


Figure 7. The estimated $\delta\beta$ between different pairs of solar active and quiet regions are plotted as red crosses along with the error bars. Also shown are the primary inversion results for $\delta\Gamma_1/\Gamma_1$ (solid line) and $\delta c_T^2/c_T^2$ (dotted line) obtained by Basu, Antia, and Bogart (2004). Because the error bars of $\delta\Gamma_1/\Gamma_1$ and of $\delta c_T^2/c_T^2$ are of similar magnitude, only the former are plotted for the sake of clarity.

and the small $\delta\beta$ are related. However, we need to study a much larger sample before we can draw any definite conclusions about the relation between flaring activity and $\delta\beta$ in the shallow subsurface layer. Another noticeable feature is that in the region below approximately $0.985R_\odot$, $\delta\beta$ becomes negative. The magnitude of this negative $\delta\beta$ in the deeper region is often comparable to that of the positive $\delta\beta$ above $0.985R_\odot$.

Hence, the results indicate that the strongest magnetic effects, which we define as the largest change in β , in ARs are generally located in a shallow region above approximately $0.985R_{\odot}$ and that the effect of magnetic fields (*i.e.*, β) in ARs become smaller than β in QSs in the deeper layers. In addition, the roughly comparable magnitudes of near-surface and deeper-layer $|\delta\beta|$ seem to imply that the stronger the AR is at the surface the smaller its β is in the deeper layers. However, it could also be that the QSs chosen to pair with the weaker ARs have larger β than the QSs chosen for the stronger ARs.

Because β is defined as the ratio between magnetic pressure and gas pressure ($P_{\text{mag}}/P_{\text{gas}}$), it is an indicator of the competition between the magnetic and gas effects. Hence, the magnitude of β simply indicates whether the gas or magnetic effects dominate in a region but not the actual magnitude of the magnetic fields. In other words, a smaller β could result from either a genuine weaker magnetic pressure or a greater gas pressure.

6. Interpretation of Inferred Results

To verify the possibilities proposed in the previous section, we examined $\delta\beta$ between regions that have different MAIs and/or are observed at different times and/or locations. The main goal is to probe the distribution profiles of β beneath an AR and a QS. Specifically, we aim to reveal whether there is indeed non-negligible β in the QSs and how β of both ARs and QSs change over the depth. We also wish to investigate how the profile of β varies with time, location, and photospheric magnetic-field strength of the region observed. In addition, while we need to study more cases to confirm whether ARs with prolific flares are often linked to small surface β , we wish to propose and discuss possible connections between the flaring activities and the subsurface β .

The regions paired for this investigation are: AR 9393 (2001 March, MAI = 241.6G) versus AR 9026 (2000 June, MAI = 146.6G), AR 9906 (2002 April, MAI = 125.8G) versus AR 8518 (1999 April, MAI = 53.2G), AR 9914 (2002 April, MAI = 86.9G) versus AR 8040 (1997 May, MAI = 19.9G), and AR 9914 versus AR 9904 (2002 April, MAI = 23.3G). For each pair, we computed the differences between the active regions (*i.e.*, AR1–AR0) and between their companion quiet regions (*i.e.*, QS1–QS0). We also computed the difference of AR1–QS0 so that the consistency of the results can be checked.

$\delta\beta$ of AR1–AR0 is to investigate whether or not the distribution of β differs between different ARs. The examination of $\delta\beta$ between two QSs is firstly to verify the non-negligible magnitude of β suggested by the results in Figures 6 and 7 and secondly to determine whether the magnetic fields in QSs are uniform or different for the different quiet regions. The results are shown in Figures 8 and 9. The top and bottom rows illustrate the differences between different ARs and between different QSs, respectively. The results of AR1–QS0 for the consistency check are plotted in the middle row.

6.1. Magnetic Effects beneath Active Regions

We can see from the top row of Figures 8 and 9 that in the region below approximately $0.985R_{\odot}$, the β of ARs with larger MAI is indeed smaller than that of ARs with

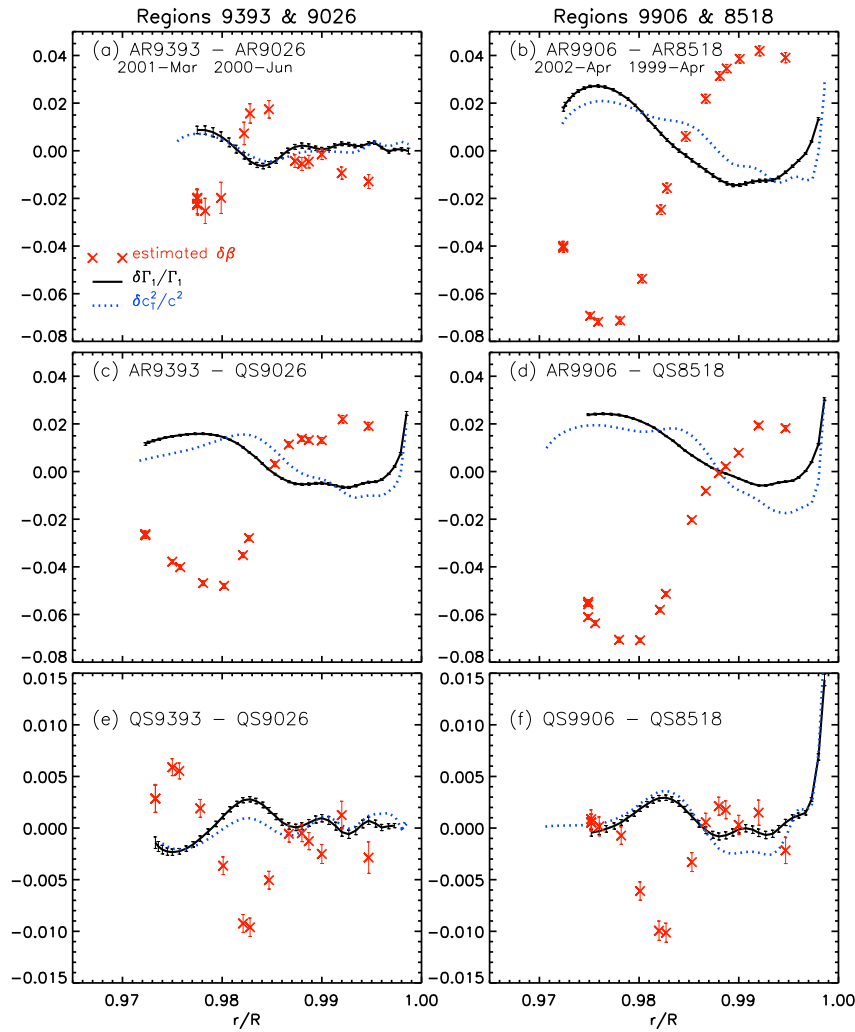


Figure 8. The inversion results and the estimated $\delta\beta$ between different regions, as denoted in the plots. The date of observation is indicated under each corresponding region. The first row displays the results between two different active regions (ARs), the second row is between one of the ARs and the quiet-Sun region (QS) of the other one, and the bottom row shows the QS of the two active regions.

smaller MAI. The comparison of different Qs as illustrated in the bottom row shows that β in these Qs does not have explicit correlation with MAI of their companion ARs. For instance, while QS 9906 is weaker than QS 8518, QS 9914 is clearly stronger than QS 8040.

A tentative picture of the magnetic structure beneath an AR that we can conjure up from these results is that the magnetic effects of the ARs are most prominent

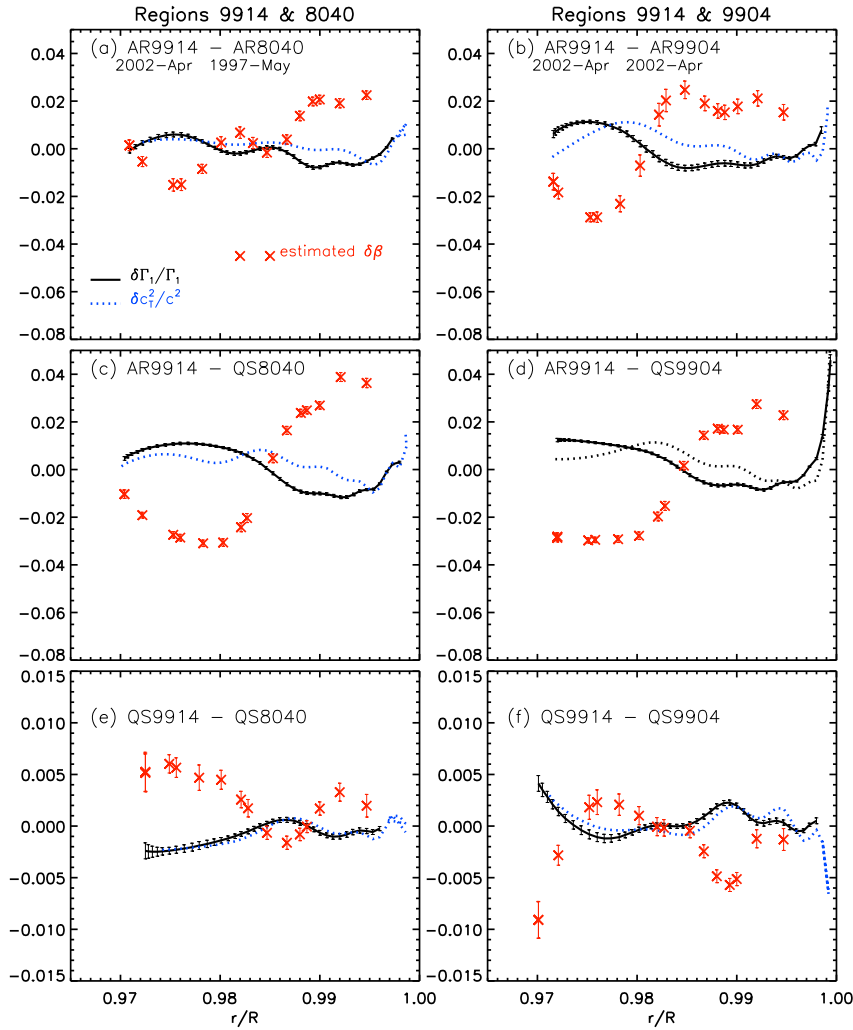


Figure 9. The inversion results and the estimated $\delta\beta$ between different regions, as denoted in the plots. The date of observation is indicated under each corresponding region. The first row displays the results between two different active regions (ARs), the second row is between one of the ARs and the quiet-Sun region (QS) of the other one, and the bottom row shows the QS of the two active regions.

in a shallow region above $0.985R_{\odot}$. In the deeper layers, the effects drop off more significantly in a strong AR than in a weak one. The reason could be that the magnetic fields near the surface reduce the convective motion and thus the gas pressure and density in the region, which can lead to an increased concentration of gas density and increased gas pressure below the magnetized area. The stronger

the magnetic fields are, the higher the increased concentration of gas in the deeper layers would be. Such increased P_{gas} , therefore, could result in lower β .

6.2. Magnetic Effects beneath Quiet Regions

The first common feature we can see from the bottom row of Figures 8 and 9 is that $|\delta\beta|$ of QSs is smaller than that of ARs. In principle, there are two possibilities for the smaller $|\delta\beta|$. It could be either the *variation* or the *magnitude* of β is smaller in QSs than in ARs. We can rule out the second one because of the following reason. The magnitudes of $\delta\beta$ in the results of AR1–AR0 provide a lower limit for β in the active regions (*i.e.*, $\max(\beta_1, \beta_0) \geq |\beta_1 - \beta_0|$). The large negative $\delta\beta$ seen in all AR–QS plots in Figures 6 to 9 indicate that the deep-layer β in the quiet regions should not be smaller than that in any of the active regions. As an example, AR 9906 – AR 8518 and AR 8518 – QS 8518 imply that $\beta_{\text{AR 8518}} \geq 0.075$ and, consequently, $\beta_{\text{QS 8518}} \geq 0.075 + 0.04$. Therefore, we can deduce from the plots that there are indeed non-negligible β in the quiet regions and that the profile of β varies from region to region albeit being more uniform and stable than that in the active regions. It should be noted that the QSs were selected to precede or follow the selected ARs, and hence, this variation between QSs is probably an indication that the evolution of magnetic fields in an AR differs from AR to AR. This is confirmed by the results seen for the pair QS 9914 – QS 9904, which are QSs associated with two different active regions during the same Carrington rotation. Because of the way the QSs were selected, such studies could be used to study the evolution of active regions.

The conclusions we can deduce from the examination of QSs are that there are non-uniform and significant magnetic structures in quiet regions. Although the results seem to suggest that the temporal variation is greater in the deeper layers than in the shallower layers, the number of our test group is too small to draw a definite conclusion.

6.3. The Anomaly in AR 9026 and AR 9393

Next, we would like to address the small inferred $\delta\beta$ in the two ARs (AR 9026 and AR 9323) that have the highest MAI and flare number among our studied regions. As the number of such cases in our current data set is too small for us to deduce statistically valid statements, we shall only propose in the following several possible explanations based on relevant theories and recent observational results:

i) P_{gas} is higher in the ARs with higher flaring activities, which leads to smaller β :

Observations have shown that the magnetic fields at the photosphere level remain roughly unchanged before and after flaring events, which means that the magnetic pressure ($P_{\text{mag}} \equiv B^2/8\pi$) should not be affected much by the flares. Hence, the small β is more likely due to an increase in gas pressure and density in the shallow layers. One possible explanation for the increased gas density is that the amount of flux coming up from the convection zone may be larger in the flaring active regions than in the non-flaring ones. Based on the storage model, which is a commonly accepted solar eruption model, the emerging flux accompanied with foot-point movements of coronal field lines can cause magnetic stress to build up in the corona and eventually lead to eruption (Priest and Forbes 2000; Lin, Li, and Basu 2003). Another possible source of the increased gas density is from the material flowing down from the corona after

the flares. However, although it has indeed been reported by helioseismology that some large flares can cause detectable ripples at the photospheric level (Kosovichev and Zharkova 1995, 1998; Zharkova and Kosovichev 1998), the mass flow from the corona, where the plasma density is approximately 10^8 times smaller than that at the photosphere, is usually insufficient to affect surface P_{gas} (hence β) by a factor of two or three, as suggested by our results (*cf.* Figure 7). In addition, observations have found that although up-flows and down-flows happen consecutively at the chromospheric level right after a flare, the temperature and gas density eventually return to the quiet-Sun values (*e.g.*, Raftery *et al.* (2008)). Based on the conservation of mass, we may expect similar situation also occur at the photosphere level.

ii) The relation between $\delta\beta$ and $\delta\Gamma_1/\Gamma_1$ derived from our models may not be suitable for the shallow layers of such highly dynamic and eruptive ARs:

In our models, the only source to affect Γ_1 is the magnetic field. However, in an explosive active region, where many dynamic activities take place, the variations in Γ_1 can come from many sources. Specifically, during a flaring event, the material in the low atmosphere is heated by the energetic particles coming down from the corona. While the total mass of the down-flow material is small relative to the photospheric density, the heating and the interaction with the energetic particles can change the state of ionization, entropy, and even the equation of state itself at the surface layer. All of these effects can change Γ_1 , and thus become part of the source for the $\delta\Gamma_1/\Gamma_1$ in our solar data. As a result, $\delta\beta$ inferred from the relation derived from the models without these effects may not reflect the actual value. For instance, the heating may counter-act the cooling effects from the magnetic fields and cause a smaller magnitude of $\delta\Gamma_1/\Gamma_1$, which leads to a smaller inferred $\delta\beta$ at the surface. In contrast, in the deeper region where the effect of the energetic particles is less and the thermal structure is better described by the structure of our models, the inferred $\delta\beta$ would be closer to the actual value, which could be the reason why the deeper-layer $\delta\beta$ of AR 9026 and AR 9393 is a factor of two to four larger than the surface-layer values.

The above hypotheses may be verified by studying a number of active-region pairs of which both have similar MAIs but one has many flares and the other has zero flares. This exercise would first confirm whether the small β near the surface is indeed a general trend in the flaring ARs. If it is positively confirmed, a large $|\delta\beta|$ in the deep layers would be an indication that there is likely to be emerging flux in the flaring ARs to cause the small β . In contrary, if we find that $|\delta\beta|$ is small in the deep layers, it implies that there is no significant difference in the magnetic structure between flaring and non-flaring ARs, and, therefore, our second hypothesis may be the explanation.

7. Modeling Subsurface Magnetic Structure

After confirming the reliability of our strategy, we ventured to investigate if we may be able to tune our simple one-dimensional magnetic models to reproduce the main features commonly seen in the inversion data. Specifically, the two main features we aim to reproduce are $\delta c_T^2/c_T^2 - \delta\Gamma_1/\Gamma_1$ being positive above $\approx 0.985R_\odot$ but negative below that, and an opposite profile for $\delta\Gamma_1/\Gamma_1$, that is, negative close to the surface but positive in the deeper layers. To produce positive $\delta c_T^2/c_T^2 - \delta\Gamma_1/\Gamma_1$

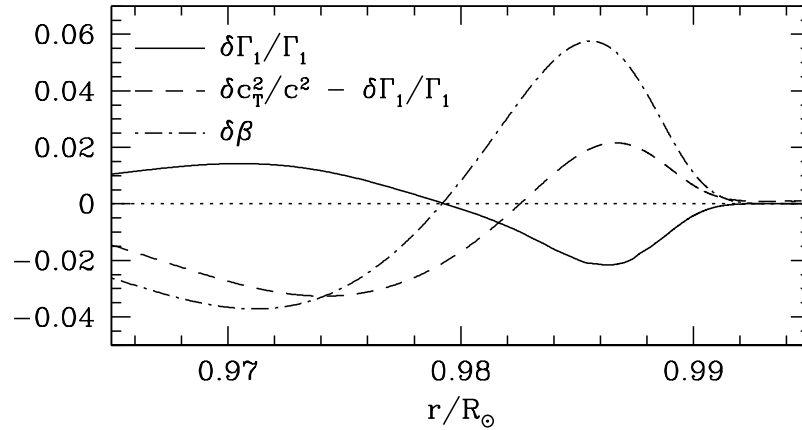


Figure 10. $\delta\Gamma_1/\Gamma_1$ and $\delta c_T^2/c^2 - \delta\Gamma_1/\Gamma_1$ between two models. The models were selected such that the relative differences qualitatively mimic those seen between solar active and quiet regions. Also shown is $\delta\beta$ between the two models.

that resemble the inversion results, our study indicates that the magnetic fields must be both strong and concentrated. To create a large, positive $\delta\Gamma_1/\Gamma_1$ commonly seen between $0.97R_\odot$ and $0.985R_\odot$, the models suggest that there has to be a negative $\delta\beta$ in that region. This can be seen in Figure 10. Although the shifting of ionization zones can also produce a positive $\delta\Gamma_1/\Gamma_1$, such changes are always localized around the ionization zone, and the magnitudes of the changes are much smaller than what is observed. Hence, our results imply that the quiet regions, which have been considered as the non-magnetic references in the inversions, could in fact contain non-negligible magnetic pressure in the deep layers.

8. Summary

The aim of this investigation was to find a practical way to determine the thermal and magnetic structure under active regions from sound speed and Γ_1 results obtained by inverting frequency differences between active and quiet regions. We have shown that “sound speed” results obtained by inverting frequency differences between active and quiet regions of the Sun represent the “wave speed” ($c_T \equiv \sqrt{\Gamma_1 P_T / \rho}$) and not the sound speed ($c_g \equiv \sqrt{\Gamma_1 P_{\text{gas}} / \rho}$) or the Alfvén speed. Thus the results cannot be interpreted as being caused by differences in either temperature or magnetic fields alone. A combination of the two is needed to interpret the results correctly.

Using solar models with magnetic fields, we have determined a simple relationship between $\delta\Gamma_1/\Gamma_1$, which is the relative difference of adiabatic index, and $\delta\beta$ ($\beta \equiv P_{\text{mag}}/P_{\text{gas}}$). $\delta\Gamma_1/\Gamma_1$ was chosen for this work because its feature is well confined in the region of magnetic fields and because it can be obtained unambiguously from inversions. We have had to derive a separate relationship between the two quantities at each depth because the process of ionization, which changes Γ_1 , varies with depth. The $\delta\beta - \delta\Gamma_1/\Gamma_1$ relation can then be used to infer the subsurface $\delta\beta$. The determined $\delta\beta$, along with inversion results of $\delta c_T^2/c_T^2$ and $\delta\Gamma_1/\Gamma_1$, can be used to determine

$\delta c_g^2/c_g^2$ and $(\delta T/T - \delta\mu/\mu)$, provided that $\delta P_{\text{gas}}/P_{\text{gas}}$ between two structures is negligible (*i.e.*, $\delta P_{\text{gas}}/P_{\text{gas}} \ll 1$). This method has been validated by using models. However, as the assumption $\delta P_{\text{gas}}/P_{\text{gas}} \ll 1$ may not be suitable in the Sun, we only present in this paper $\delta\beta$ revealed by applying the method to the solar results obtained by Basu, Antia, and Bogart (2004).

The application of $\delta\beta - \delta\Gamma_1/\Gamma_1$ relation to the solar inversion results shows that, as expected, different active regions behave quite differently. Nevertheless, for all regions studied, $\delta\beta$ is always positive immediately below the surface ($r > 0.985R_\odot$) but negative at deeper regions, which implies that the inward decrease of β is faster in an AR with larger MAI than in one with smaller MAI.

The reason for the faster decrease of β under stronger ARs could be because the stronger magnetic fields near the surface suppress convection more, resulting in a larger build-up of gas (*i.e.*, higher density and gas pressure), which leads to lower $\beta \equiv P_{\text{mag}}/P_{\text{gas}}$ in the deeper regions. It also appears that the so-called quiet regions have deep-seated magnetic effects.

We find that the near-surface β of AR 9026 and AR 9393, which have largest number of flares among all studied regions, is anomalously low. We propose two possible reasons to explain the phenomena. One is that P_{gas} is larger in the flaring ARs because, as some theories have proposed, flares might be caused by the larger amount of flux coming from the convection zone. Another possibility is that the relation between $\delta\beta$ and $\delta\Gamma_1/\Gamma_1$ derived from our models may not be suitable for the shallow layers of such highly dynamic and eruptive ARs, where the variations in Γ_1 can now come from many sources rather than solely from the magnetic fields as in our models. In either case, the inferred $\delta\beta$ may not reflect the actual value.

Our attempt to reproduce the active-region profiles of $\delta\Gamma_1/\Gamma_1$ and $\delta c_T^2/c_T^2$ suggests that the magnetic fields must be both strong and concentrated in order to produce the positive $\delta c_T^2/c_T^2$ that is seen in the deeper layers. Additionally, the large, positive $\delta\Gamma_1/\Gamma_1$ commonly seen between $0.97R_\odot$ and $0.985R_\odot$ can only be caused by a negative $\delta\beta$ in that region. The shifting of ionization zones does not produce matching magnitudes and locations of the positive $\delta\Gamma_1/\Gamma_1$.

Acknowledgments

We wish to thank the referee for detailed comments on this paper. CHL wishes to thank Dr. Shaun Bloomfield, Prof. Douglas Gough, and Ms. Claire Raftery for helpful discussion. This work utilizes data from the Solar Oscillations Investigation / Michelson Doppler Imager (SOI/MDI) on the *Solar and Heliospheric Observatory (SOHO)*. SOHO is a project of international cooperation between ESA and NASA. MDI is supported by NASA grant NAG5-8878 to Stanford University. This work is partially supported by NSF grants ATM 0348837 and ATM 0737770 as well as NASA grant NNG06D13C to SB. CHL is also supported by an ESA/PRODEX grant administered by Enterprise Ireland.

References

- Alexander, D.R., Ferguson, J.W.: 1994, *Astrophys. J.* **437**, 879.,
 Antia, H.M., Basu, S.: 1994, *Astron. Astrophys. Supp.* **107**, 421.

- Bahcall, J.M., Pinsonneault, M.H.: 1992, *Rev. Mod. Phys.* **64**, 885.
- Basu, S., Antia, H.M., Bogart, R.S.: 2004, *Astrophys. J.* **610**, 1157.
- Basu, S., Antia, H.M., Bogart, R.S.: 2007, *Astrophys. J.*, **654**, 1146.
- Demarque, P., Guenther, D.B., Li, L.H., Mazumdar, A., Straka, C.W.: 2007, *Astrophys. Space Sci.*, **316**, 31. <http://www.springerlink.com/content/5025w516123252q4/>
- Duvall, T.L. Jr., Jefferies, S.M., Harvey, J.W., Pomerantz, M.A., 1993, *Nature* **362**, 430.
- Dziembowski, W.A., Pamyatnykh, A.A., Sienkiewicz, R.: 1990, *Mon. Not. Roy. Astron. Soc.* **244**, 542.
- Haber, D.A.: 2004, In: Danesy, D. (ed.), *SOHO 14 Helio- and Asteroseismology: Towards a Golden Future*, **SP-559**, ESA, Noordwijk, 676.
- Hill, F.: 1988, *Astrophys. J.* **333**, 996.
- Iglesias, C.A., Rogers, F.J.: 1996, *Astrophys. J.* **464**, 943.
- Kosovichev, A.G., Zharkova, V.V.: 1995, In: Hoeksema, J.T., Domingo, V., Fleck, B., Battrick, B. (eds.), *Fourth SOHO Workshop Helioseismology*, **SP-372-2**, ESA, Noordwijk, 341.
- Kosovichev, A.G., Zharkova, V.V.: 1998, In: Deubner, F.-L., Christensen-Dalsgaard, J., Kurtz, D. (eds.) *New Eyes to See Inside the Sun and Stars*, IAU Sympos. **185**, Kluwer, Dordrecht, 191.
- Kosovichev, A.G., Duvall, T.L. Jr., Scherrer, P.H. 2000, *Solar Phys.* **192**, 159
- Kosovichev, A.G., Duvall, T.L. Jr., Birch, A.C., Gizon, L., Scherrer, P.H., Zhao, J.: 2001, In: Wilson, A., Pallé, P.L. (eds.), *SOHO 10/GONG 2000 Workshop: Helio- and Asteroseismology at the Dawn of the Millennium*, **SP-464**, ESA, Noordwijk, 701.
- Lin, C.-H., Li, L.H., Basu, S.: 2006, In: Fletcher, K., Thompson, M.J. (eds.), *SOHO 18/GONG 2006/HELAS I: Beyond the Spherical Sun*, **SP-624**, ESA, Noordwijk, 58.
- Lin, J., Soon, W., Baliunas, S.L.: 2003, *New Astron. Rev.* **47**, 53.
- Li, L.H., Basu, S., Sofia, S., Robinson, F.J., Demarque, P., Guenther, D.B.: 2003, *Astrophys. J.* **591**, 1267.
- Li, L.H., Sofia, S.: 2001, *Astrophys. J.* **549**, 1204.
- Lydon, T.J., Sofia, S.: 1995, *Astrophys. J. Suppl.* **101**, 357.
- Patron, J., Gonzalez Hernandez, I., Chou, D.-Y., Sun, M.-T., Mu, T.-M., Loudagh, S., Bala, B., Chou, Y.-P., Lin, C.-H., Huang, I.-J., Jimenez, A., Rabello-Soares, M.C., Ai, G., Wang, G.-P., Zirin, H., Marquette, W., Nenow, J., Ehgamberdiev, S., Khalikov, S., TON Team: 1997, *Astrophys. J.* **485**, 869.
- Pijpers, F.P., Thompson, M.J.: 1992, *Astron. Astrophys* **262**, L33.
- Pijpers, F.P., Thompson, M.J.: 1994, *Astron. Astrophys* **281**, 231.
- Priest, E., Forbes, T.: 2000, In: *Magnetic Reconnection: MHD Theory and Applications*, Cambridge University Press, Cambridge, 363.
- Rabello-Soares, M.C., Basu, S., Christensen-Dalsgaard, J.: 1998, In: Korzennik, S. (ed.) *Structure and Dynamics of the Interior of the Sun and Sun-like Stars – SOHO 6/GONG 98*, **SP-418**, ESA, Noordwijk, 505.
- Raftery, C.L., Gallagher, P.T., Milligan, R.O., Klimchuck, J.A.: 2008, *Astron. Astrophys*, *submitted*
- Rogers, F.J., Nayfonov, A.: 2002, *Astrophys. J.* **659**, 750.
- Rhodes, E.J. Jr., Reiter, J., Kosovichev, A.G., Schou, J., Scherrer, P.H.: 1998, In: Korzennik, S. (ed.) *Structure and Dynamics of the Interior of the Sun and Sun-like Stars – SOHO 6/GONG 98*, **SP-418**, ESA, Noordwijk, 73.
- Schou, J.: 1999, *Astrophys. J.* **523**, L181.
- Spruit, H.C.: 1981, *Astron. Astrophys* **98**, 155.
- Trujillo Bueno, J., Shchukina, N., Asensio Ramos, A.: 2004, *Nature* **430**, 326.
- Zharkova, V.V., Kosovichev, A.G.: 1998, In: Korzennik, S. (ed.) *Structure and Dynamics of the Interior of the Sun and Sun-like Stars – SOHO 6/GONG 98*, **SP-418**, ESA, Noordwijk, 661.

